Journal of ELECTRONIC MATERIALS, Vol. 46, No. 5, 2017
DOI: 10.1007/s11664-017-5366-3

High-Temperature Thermoelectric Properties of Perovskite-Type $Pr_{0.9}Sr_{0.1}Mn_{1-x}Fe_xO_3$ ($0 \le x \le 1$)

H. NAKATSUGAWA,[1,4] M. SAITO,[2] and Y. OKAMOTO[3]

1.—Yokohama National University, 79-5 Tokiwadai, Hodogaya-Ku, Yokohama 240-8501, Japan. 2.—Kanagawa University, 3-27-1 Rokkakubashi, Kanagawa-ku, Yokohama 221-8686, Japan. 3.—National Defense Academy, 1-10-20 Hashirimizu, Yokosuka 239-8686, Japan. 4.—e-mail: naka@ynu.ac.jp

Polycrystalline samples of $Pr_{0.9}Sr_{0.1}Mn_{1-x}Fe_xO_3$ ($0 \le x \le 1$) have been synthesized using a conventional solid-state reaction method, and the crystal structure studied at room temperature. The magnetic susceptibility was measured from 5 K to 350 K. The electrical resistivity, Seebeck coefficient, and thermal conductivity were investigated as functions of temperature below 850 K. For all samples, the perovskite structure at room temperature exhibited orthorhombic *Pbnm* phase. While the $Pr_{0.9}Sr_{0.1}MnO_3$ ($x = 0$) sample exhibited ferromagnetic-like ground state below $T_C = 145$ K (Curie temperature), the ferromagnetic transition temperature T_C decreased with increasing x. The Seebeck coefficient of the samples with $0 \le x \le 0.8$ decreased with increasing temperature because of double-exchange interaction of Mn ions. In fact, the carrier type for $x = 0$ changed from hole-like to electron-like behavior above 800 K. On the other hand, the samples with $x \ge 0.9$ showed large positive Seebeck coefficient over the entire temperature range, indicating that the low-spin state of Fe ions dominated the electronic structure for this x range. In particular, the sample with $x = 1$ exhibited p-type thermoelectric properties with relatively high Seebeck coefficient, moderate electrical resistivity, and low thermal conductivity. Thus, the sample with $x = 1$ showed power factor of 20 μW m^{-1} K^{-2} at 850 K leading to ZT of 0.024 at this temperature, indicating that hole-doped perovskite-type iron oxide is a good candidate high-temperature thermoelectric p-type oxide.

Key words: Thermoelectric properties, magnetic properties, perovskite structure, ZT value, spin state, Heikes formula

INTRODUCTION

Since the layered cobalt oxide Na_xCoO_2 was discovered to have large Seebeck coefficient (S = 100 μV K^{-1}) and low electrical resistivity (ρ = 20 mΩm) at room temperature, oxides have been intensively studied as possible high-temperature thermoelectric materials for use above 1000 K[1]; For example, the misfit-layered cobalt oxide $Ca_3Co_4O_9$, exhibiting S = 130 μV K^{-1}, ρ = 150 mΩm, and κ = 1.0 W mK^{-1} at room temperature, where κ is the thermal conductivity, has been studied as a potential thermoelectric p-type oxide.[2] In the case of Al-doped ZnO, which shows band conduction, the carrier concentration increases and the n-type thermoelectric properties improve with increasing Al content.[3] The perovskite-type oxide $Ba_{1-x}Sr_xPbO_3$ ($0 \le x \le 1$), which also shows band conduction, has high carrier mobility and n-type thermoelectric properties that improve with increasing x.[4] Another perovskite-type oxide, $CaMnO_3$, was found to have high carrier mobility and good n-type thermoelectric properties upon partial substitution at Ca sites by lanthanoid cations, due to the resulting increase in the distance between polaron hopping sites.[5]

Power generation using an oxide thermoelectric module consisting of p-type $Ca_{2.7}Bi_{0.3}Co_4O_9$ and

(Received May 27, 2016; accepted February 9, 2017; published online February 24, 2017)

n-type $La_{0.9}Bi_{0.1}NiO_3$ has been published.[6] Indeed, charging of a mobile phone has been achieved using this oxide thermoelectric module, although the maximum efficiency η_{max} was ≤1.4%.[7] Urata et al.[8] also built thermoelectric modules consisting of *p*-type $Ca_{2.7}Bi_{0.3}Co_4O_9$ and *n*-type $CaMn_{0.98}Mo_{0.02}O_3$, achieving η_{max} of 2.0%. However, the *n*-type elements were destroyed by thermal stress with the substrate.[8] Therefore, a thermoelectric module consisting of *p*–*n* elements with small linear thermal expansion coefficient difference is desirable. Thus, our group has focused efforts on the study of perovskite-type oxides, which can form both *n*- and *p*-type conductors, and recently identified $Pr_{0.9}Sr_{0.1}MnO_3$ as a potential thermoelectric *p*-type oxide, despite its low *ZT* of 0.0035 at 468 K.[9]

Perovskite-type oxides such as titanate,[10] manganate,[5] ferrate,[11] and cobaltate[12] exhibit large Seebeck coefficient, an essential requirement for thermoelectric materials. These large *S* values result from strong interactions between spin states, orbitals, charges, and crystal structure. Koshibae et al.[13] proposed that the Heikes formula based on a localized picture can give the high-temperature limit of *S* in 3*d* transition-metal oxides. When the degeneracy of spin and/or orbital degrees of freedom in 3*d* transition-metal ions is high, the Heikes formula can be expected to yield large *S*.[9] Thus, control over the spin and/or orbital states of 3*d* transition-metal ions would enable improvement of *ZT* in thermoelectric oxides. From this perspective, electron-doped manganates have shown interesting *n*-type thermoelectric properties at high temperatures.[5,14–20] Though perovskite-type Mn oxides have already been extensively researched due to their colossal magnetoresistance (CMR) at low temperature,[21,22] which has been attributed to competition between the double-exchange (DE) interaction[23] and Jahn–Teller (JT) distortion of the octahedral MnO_6 structure,[24] we focused on the *n*-type thermoelectric properties at high temperatures. In the case of polycrystalline *n*-type $Ca_{0.9}Yb_{0.1}MnO_3$, Flahaut et al.[19] reported *ZT* = 0.16 at 1000 K in air.

While remarkably little is known about the *p*-type thermoelectric properties of perovskite-type oxides, hole-doped perovskite-type Fe oxides exhibit *p*-type thermoelectric properties at high temperature. Indeed, Iijima and Murayama[11] reported *ZT* of 0.075 at 1273 K for polycrystalline *p*-type $La_{0.95}Sr_{0.05}FeO_3$. Thus, it is necessary to perform detailed studies of the *p*-type thermoelectric properties of both hole-doped perovskite-type Mn and Fe oxides. In the present study, we prepared polycrystalline samples of $Pr_{0.9}Sr_{0.1}Mn_{1-x}Fe_xO_3$ ($0 \le x \le 1$), and investigated their *p*-type thermoelectric properties considering the effects of Fe doping on both the magnetic properties and crystal structure, to elucidate the *ZT* of these materials. From both the magnetic properties and crystal structure of $Pr_{0.9}Sr_{0.1}Mn_{1-x}Fe_xO_3$ ($0 \le x \le 1$), we determined both the ionic valences and spin states of the 3*d* transition-metal ions, and estimated the high-temperature limit of *S* using the Heikes formula. Thus, we also present a more efficient approach to identify promising thermoelectric *p*-type oxides.

EXPERIMENTAL PROCEDURES

Polycrystalline samples of $Pr_{0.9}Sr_{0.1}Mn_{1-x}Fe_xO_3$ ($0 \le x \le 1$) were synthesized using a conventional solid-state reaction method: Stoichiometric mixtures of Pr_6O_{11} (99.9%, 3 N, Wako Pure Chemical Industries, Ltd.), $SrCO_3$ (99.99%, 4 N, Wako Pure Chemical Industries, Ltd.), Fe_2O_3 (99.9%, 3 N, Wako Pure Chemical Industries, Ltd.), and Mn_2O_3 (99.9%, 3 N, Kojundo Chemical Laboratory Co., Ltd.), mixed in an agate mortar with ethanol, were calcined at 1273 K for 24 h in air.[9] The calcined powders were pressed into pellets under 16 MPa of pressure and sintered in pure flowing oxygen gas at 1573 K for 48 h.[9] The pellets were cooled to 300 K in the furnace.[9] Powder x-ray diffraction (XRD) data were collected with a diffractometer (RINT2500, Rigaku Co.), using Cu K_α (λ = 1.542 Å) radiation with a pyrolytic graphite monochromator at room temperature.[9] Crystal structure parameters were refined by Rietveld analysis using RIETAN-FP software[25] with XRD data in the 2θ range from 10° to 90° in steps of 0.02°.[9]

The resistivity ρ was measured by van der Pauw technique in the temperature range from 80 K to 395 K using commercial apparatus (ResiTest8300, TOYO Co.) and by the direct-current four-probe method in the temperature range from 300 K to 850 K using an apparatus built in house.[9] The Seebeck coefficient *S* was measured using a steady-state technique in the temperature range from 80 K to 395 K using ResiTest8300 apparatus (TOYO Co.) and in the temperature range from 300 K to 850 K using home-built apparatus.[9] *S* was measured by least-squares approximation to a plot of thermoelectromotive force versus temperature difference, from which the contribution of lead wires was subtracted.[9] The thermal conductivity κ was calculated from the thermal diffusivity α, the specific heat at constant volume C_V, and the bulk density *d*, using the relationship $\kappa = d\alpha C_V$.[9] The bulk density was measured by the Archimedes method at room temperature using a specific gravity measurement kit (SMK-401, Shimadzu Co.).[9] The relative density of all samples was measured to lie approximately in the range from 90% to 95%.[9] The specific heat was determined by differential scanning calorimetry (DSC) in the temperature range from 303 K to 323 K using X-DSC7000 apparatus (Hitachi High-Tech Science Co.).[9] The thermal diffusivity was measured at room temperature and from 573 K to 973 K in steps of 100 K, using the laser flash method (TC-7000, ULVAC-RIKO Co.).[9] The magnetic susceptibility χ was measured in the temperature range from 5 K to 350 K using a

superconducting quantum interference device (SQUID) magnetometer (MPMS, Quantum Design, Inc.) under zero-field cooling (ZFC) conditions at magnetic field of 1 T during the warming process.[9]

RESULTS AND DISCUSSION

Our XRD data confirmed that all specimens were single phase with orthorhombic perovskite structure (space group *Pbnm*) for $Pr_{0.9}Sr_{0.1}Mn_{1-x}Fe_xO_3$ ($0 \le x \le 1$), as shown in Fig. 1 and Table I. The structural parameters were determined by the Rietveld refinement method using the RIETAN-FP program (Table I).[25] In this work, the isotropic atomic displacement parameters B were fixed in the analysis at 0.5 for both Pr/Sr sites and Mn/Fe sites, and 1.0 for both apical oxygen (O1) sites and equatorial oxygen (O2) sites.[9] A split pseudo-Voigt function was used to fit the Bragg peak shapes.[9] The Rietveld refinement's weighted profile reliability factors R_{wp} ranged from about 8% to 18%, indicating good fit between observed and calculated intensities.

Although the ionic radii of the high-spin (HS) Mn^{3+} and HS Mn^{4+} ions are slightly larger than those of the low-spin (LS) Fe^{3+} and LS Fe^{4+} ions, respectively (0.645 Å for HS Mn^{3+}, 0.53 Å for HS Mn^{4+}, 0.55 Å for LS Fe^{3+}, and 0.585 Å for LS Fe^{4+}),[26] it can be seen that lattice parameters a and c slightly increase with increasing Fe content x, as shown in Fig. 2. The Mn/Fe–O1/O2 distances and the Mn/Fe–O1/O2–Mn/Fe angles are summarized in Table I, together with the Goldschmidt tolerance factor[27] and the bond valence sum (BVS).[28] The Goldschmidt tolerance factor for the perovskite structure ABO_3 is defined as $(r_A + r_O)/\sqrt{2}(r_B + r_O)$ and represents a structural parameter describing geometric distortion, where r_n (n = A, B, and O) are the average ionic radii of the A, B, and oxygen sites, respectively. On the other hand, the BVS of A and B sites in ABO_3 are defined as $\sum_j \exp[(r_0 - r_{ij})/0.37\ \text{Å}]$, where r_0 and r_{ij} are the bond valence parameter and observed bond length between cation and oxygen, respectively. In addition, the r_0 values used for Pr^{3+}, Sr^{2+}, Mn^{3+}, Mn^{4+}, Fe^{3+}, and Fe^{4+} are 2.138 Å, 2.118 Å, 1,732 Å, 1.750 Å, 1.751 Å, and 1.765 Å, respectively. As shown in Table I, despite the decrease in r_B, the tolerance factor increased with increasing x because r_A remained constant, indicating that lattice parameters a and c increased slightly. On the other hand, the BVS of A and B sites was observed to be about 2.9 and 3.1, corresponding to the nominal ionic valences of the cations, respectively. This indicates, therefore, that the contribution of the redox activity of praseodymium, i.e., Pr^{3+}/Pr^{4+}, would be negligible in $Pr_{0.9}Sr_{0.1}Mn_{1-x}Fe_xO_3$ ($0 \le x \le 1$).

Figure 3 shows the temperature variation of the direct-current (dc) susceptibility $\chi - \chi_0$ under magnetic field of 1 T for $0 \le x \le 1$, measured during the process of warming to room temperature after ZFC to

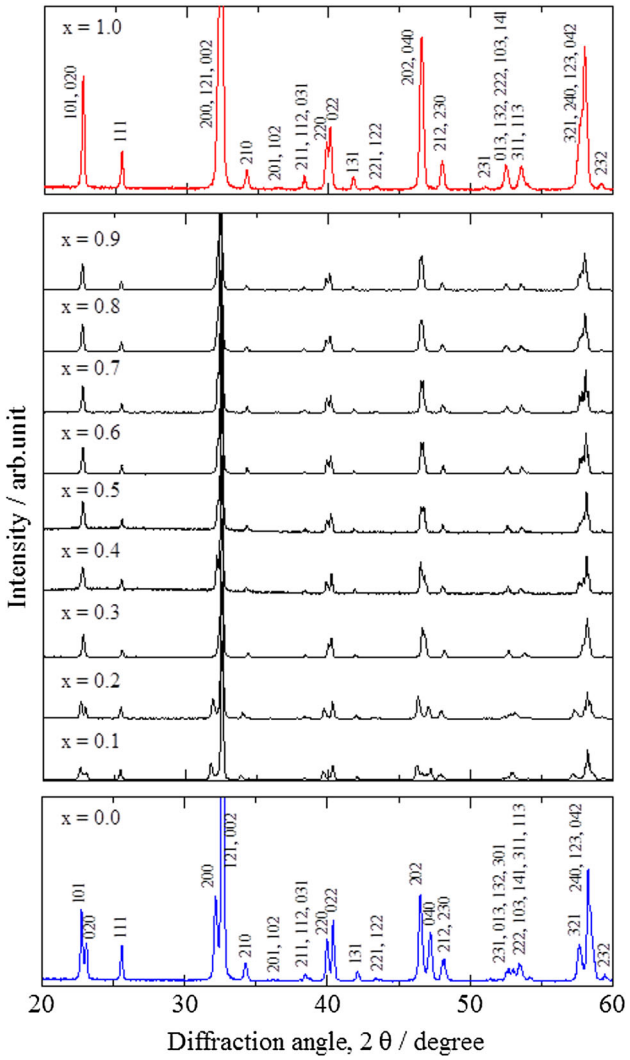

Fig. 1. X-ray diffraction patterns of $Pr_{0.9}Sr_{0.1}Mn_{1-x}Fe_xO_3$ ($0 \le x \le 1$) at room temperature.

5 K, where χ_0 is the contribution of the temperature-independent magnetic susceptibility. The temperature dependence of $\chi - \chi_0$ suggests that ferromagnetism is suppressed with increasing x. Figure 4 shows the inverse of the dc susceptibility $(\chi - \chi_0)^{-1}$ versus temperature T for specimens with $0 \le x \le 1$, where the curves show a linear relationship in the high-temperature paramagnetic (PM) range. PM properties can be expressed as $\chi - \chi_0 = C/(T - \Theta)$, where C is the Curie constant and Θ is the Curie temperature.[9] The PM properties summarized in Table II were obtained by plotting $(\chi - \chi_0)^{-1}$. The effective magnetic moment of each B site, μ_{eff}, was then established using the observed C value, i.e.,

$$\mu_{eff} = 2\sqrt{S'(S'+1)}\mu_B = \sqrt{\frac{3k_B C}{N_A}}, \qquad (1)$$

where k_B, μ_B, N_A, and S' are the Boltzmann constant, the Bohr magnetron, Avogadro's number,

Table I. Crystal structure parameters of $Pr_{0.9}Sr_{0.1}Mn_{1-x}Fe_xO_3$ ($0 \le x \le 1$) at room temperature

Sample		$Pr_{0.9}Sr_{0.1}MnO_3$	$Pr_{0.9}Sr_{0.1}Mn_{1-x}Fe_xO_3$									$Pr_{0.9}Sr_{0.1}FeO_3$
Composition, x		**0**	**0.1**	**0.2**	**0.3**	**0.4**	**0.5**	**0.6**	**0.7**	**0.8**	**0.9**	**1**
Space group		*Pbnm*	*Pbnm*	*Pbnm*	*Pbnm*	*Pbnm*	*Pbnm*	*Pbnm*	*Pbnm*	*Pbnm*	*Pbnm*	*Pbnm*
Goldschmidt tolerance factor		0.906	0.910	0.911	0.914	0.920	0.922	0.930	0.930	0.935	0.939	0.940
BVS of A site in ABO_3: valence units (v.u.)		2.97	2.95	2.94	2.89	2.95	2.92	2.90	2.98	2.92	2.91	2.89
BVS of B site in ABO_3: valence units (v.u.)		3.07	3.12	3.08	3.15	3.16	3.12	3.12	3.09	3.13	3.14	3.13
a (Å)		5.4693(4)	5.4650(6)	5.4690(4)	5.4746(3)	5.4763(3)	5.4790(4)	5.4799(2)	5.4813(2)	5.4832(2)	5.4852(2)	5.4906(5)
b (Å)		5.5542(4)	5.5987(5)	5.5843(4)	5.5159(3)	5.5443(3)	5.5371(4)	5.5345(2)	5.5364(2)	5.5371(2)	5.5365(2)	5.5462(5)
c (Å)		7.6874(6)	7.6761(7)	7.7048(6)	7.7394(4)	7.7480(5)	7.7557(5)	7.7605(3)	7.7653(3)	7.7676(3)	7.7725(4)	7.7827(7)
V (Å^3)		233.53(3)	234.86(4)	235.32(3)	233.71(2)	235.25(2)	235.29(2)	235.36(1)	235.65(1)	235.83(2)	236.04(2)	237.00(3)
$a/\sqrt{2}$ (Å)		3.8674	3.8643	3.8672	3.8711	3.8723	3.8742	3.8749	3.8759	3.8772	3.8786	3.8824
$b/\sqrt{2}$ (Å)		3.9274	3.9589	3.9487	3.9003	3.9204	3.9153	3.9135	3.9148	3.9153	3.9149	3.9218
$c/2$ (Å)		3.8437	3.8381	3.8524	3.8697	3.8740	3.8779	3.8803	3.8827	3.8838	3.8863	3.8914
Pr/Sr, La/Sr	x	−0.0071(2)	0.0074(4)	0.0082(3)	0.0058(3)	0.0060(7)	0.0072(5)	0.0073(2)	0.0076(2)	0.0080(2)	0.0077(2)	0.0079(2)
	y	0.0396(1)	−0.0451(2)	−0.0440(1)	−0.0367(1)	−0.0374(2)	−0.0394(2)	−0.0381(1)	−0.0376(1)	−0.0391(1)	−0.0388(1)	−0.0398(1)
	z	1/4	1/4	1/4	1/4	1/4	1/4	1/4	1/4	1/4	1/4	1/4
	B (Å^2)	0.5	0.5	0.5	0.5	0.5	0.5	0.5	0.5	0.5	0.5	0.5
	g	1.0	1.0	1.0	1.0	1.0	1.0	1.0	1.0	1.0	1.0	1.0
Mn, Fe	x	1/2	1/2	1/2	1/2	1/2	1/2	1/2	1/2	1/2	1/2	1/2
	y	0	0	0	0	0	0	0	0	0	0	0
	z	0	0	0	0	0	0	0	0	0	0	0
	B (Å^2)	0.5	0.5	0.5	0.5	0.5	0.5	0.5	0.5	0.5	0.5	0.5
	g	1.0	1.0	1.0	1.0	1.0	1.0	1.0	1.0	1.0	1.0	1.0
O1	x	0.073(2)	−0.093(3)	−0.078(2)	−0.065(2)	−0.065(3)	−0.076(3)	−0.074(1)	−0.077(1)	−0.074(1)	−0.073(1)	−0.080(2)
	y	0.493(1)	0.505(2)	0.514(1)	0.507(1)	0.517(2)	0.511(2)	0.514(1)	0.513(1)	0.513(1)	0.514(1)	0.513(1)
	z	1/4	1/4	1/4	1/4	1/4	1/4	1/4	1/4	1/4	1/4	1/4
	B (Å^2)	1.0	1.0	1.0	1.0	1.0	1.0	1.0	1.0	1.0	1.0	1.0
	g	1.0	1.0	1.0	1.0	1.0	1.0	1.0	1.0	1.0	1.0	1.0
O2	x	0.721(1)	0.722(2)	0.721(2)	0.718(1)	0.727(3)	0.716(3)	0.713(1)	0.712(1)	0.711(1)	0.711(1)	0.711(1)
	y	0.289(1)	0.301(2)	0.290(1)	0.285(1)	0.299(2)	0.294(2)	0.287(1)	0.293(1)	0.289(1)	0.287(1)	0.289(1)
	z	0.035(1)	−0.020(2)	−0.036(1)	−0.038(1)	−0.042(1)	−0.033(1)	−0.035(1)	−0.0389(9)	−0.0371(9)	−0.037(1)	−0.034(1)
	B (Å^2)	1.0	1.0	1.0	1.0	1.0	1.0	1.0	1.0	1.0	1.0	1.0
	g	1.0	1.0	1.0	1.0	1.0	1.0	1.0	1.0	1.0	1.0	1.0
R_{wp} (%)		12.377	18.475	14.853	12.112	8.567	8.172	10.706	10.697	10.249	11.035	11.708
R_P (%)		9.442	13.252	11.084	9.084	6.581	6.187	7.478	7.308	6.832	7.503	8.298
R_R (%)		12.869	17.935	14.998	12.951	22.582	20.200	9.997	9.684	8.831	9.786	11.142
R_e (%)		5.367	6.541	6.824	7.171	5.282	5.397	6.713	6.714	6.365	6.558	7.061
R_B (%)		3.200	4.796	2.819	6.707	5.379	3.805	3.438	2.941	2.301	4.162	4.594

Table I. continued

Sample		$Pr_{0.9}Sr_{0.1}MnO_3$	$Pr_{0.9}Sr_{0.1}Mn_{1-x}Fe_xO_3$							$Pr_{0.9}Sr_{0.1}FeO_3$
Composition, x		0	0.1	0.2	0.3	0.4	0.5	0.6	0.7	0.8	0.9	1
R_F (%)		2.045	3.589	2.494	3.653	5.327	4.837	2.405	2.272	1.489	2.477	3.017
(Mn, Fe)–O1 (Å)	×2	1.963(2)	1.985(4)	1.975(2)	1.968(2)	1.972(3)	1.983(4)	1.983(2)	1.988(2)	1.985(2)	1.991(8)	1.996(2)
(Mn, Fe)–O2 (Å)	×2	1.939(9)	1.88(1)	1.93(1)	1.96(1)	1.89(1)	1.94(1)	1.981(7)	1.971(7)	1.985(7)	1.985(2)	1.987(8)
(Mn, Fe)–O2 (Å)	×2	2.032(9)	2.08(1)	2.04(1)	2.00(1)	2.10(1)	2.03(1)	1.995(7)	2.020(6)	1.998(7)	1.992(7)	1.997(9)
(Mn, Fe)–O1–(Mn, Fe) (°)		156.3(6)	150(1)	154.3(7)	158.7(7)	158(1)	155(1)	155.9(5)	155.0(5)	155.8(5)	156.1(5)	154.1(6)
(Mn, Fe)–O2–(Mn, Fe) (°)		157.8(4)	159.9(7)	157.2(4)	156.8(4)	154.8(6)	156.5(6)	156.6(3)	154.7(3)	155.8(3)	155.8(3)	156.6(4)

and the spin quantum number, respectively. Since the Mn/Fe ions in $Pr_{0.9}Sr_{0.1}Mn_{1-x}Fe_xO_3$ ($0 \le x \le 0.9$) are in HS Mn^{3+} ($t_{2g}^3e_g^1$), HS Mn^{4+} (t_{2g}^3), LS Fe^{3+} (t_{2g}^5), and LS Fe^{4+} (t_{2g}^4) states, respectively, the valence state of each Mn/Fe ion can be directly derived from Eq. 1. Although the nominal valence states of Mn/Fe ions for all specimens are fixed at 3.1, the majority of the trivalent and tetravalent ions at B sites change from HS Mn^{3+} and HS Mn^{4+} to LS Fe^{3+} and LS Fe^{4+}, respectively, with increasing x. Some of the trivalent ions for $x = 1$ change from LS Fe^{3+} to intermediate-spin (IS) Fe^{3+} ($t_{2g}^4e_g^1$). Table II presents χ_0, Θ, C, μ_{eff}, S', the ionic ratios of Mn/Fe ions, and the average ionic radii of A/B sites for $0 \le x \le 1$.

The temperature dependence of the electrical resistivity ρ for specimens with $0 \le x \le 1$ measured below 850 K is shown in Fig. 5. All samples showed semiconducting behavior over the whole temperature range, and the resistivity increased with increasing x. However, the resistivity decreased rapidly when x was increased from $x = 0.9$ to $x = 1$. This suggests that the low-spin sate of Fe ions dominates the electronic structure for $x \ge 0.9$ and the specimen with $x = 1$ is a good electroconductive oxide. In addition, all samples exhibited adiabatic small polaron behavior in the conduction mechanism above room temperature, as shown in Fig. 6. For small polaron hopping conduction, the carrier mobility μ exhibits thermally activated temperature dependence, i.e., $\mu \propto \exp(-W_H/k_BT)$, rather than the carrier concentration n, where W_H is the hopping energy of small polarons and n denotes the number of hopping small polarons per unit volume, i.e., $n_0 \exp(-E_g/2k_BT)$. Thus, the temperature dependence of the electrical conductivity $\sigma = en\mu$, predicted by polaron theory,[29–31] is as follows:

$$\sigma = \frac{e^2 n_0 \omega_{LO} a_0^2}{k_B T} \exp\left(-\frac{W_H + E_g/2}{k_B T}\right) = \frac{\sigma_0}{T} \exp\left(-\frac{E_\sigma}{k_B T}\right), \quad (2)$$

where n_0 is the concentration of tetravalent ions per unit volume, ω_{LO} is the optical phonon frequency, a_0 is the characteristic intersite hopping distance corresponding to the typical Mn/Fe–O–Mn/Fe distance in our samples, σ_0 is the preexponential term, and E_σ is the activation energy of the conduction process.[9]

As is clear from Table III, all σ values above 300 K are well explained by the activated conduction process. As shown in Fig. 6, the Arrhenius relationship between σT and T^{-1} above 300 K is nearly linear with slope of E_σ. Furthermore, least-mean-square fitting yielded σ_0 in the range from $10^7\ \Omega^{-1}\ m^{-1}\ K$ to $10^8\ \Omega^{-1}\ m^{-1}\ K$ by extrapolating σT to $T^{-1} \to 0$ in Fig. 6. ω_{LO} (Table III) was derived from the concentrations of tetravalent ions ($n_0 \approx 10^{27}\ m^{-3}$ to $10^{28}\ m^{-3}$), calculated from the lattice parameters and the mean Mn/Fe–O–Mn/Fe distance a_0 determined by Rietveld refinement

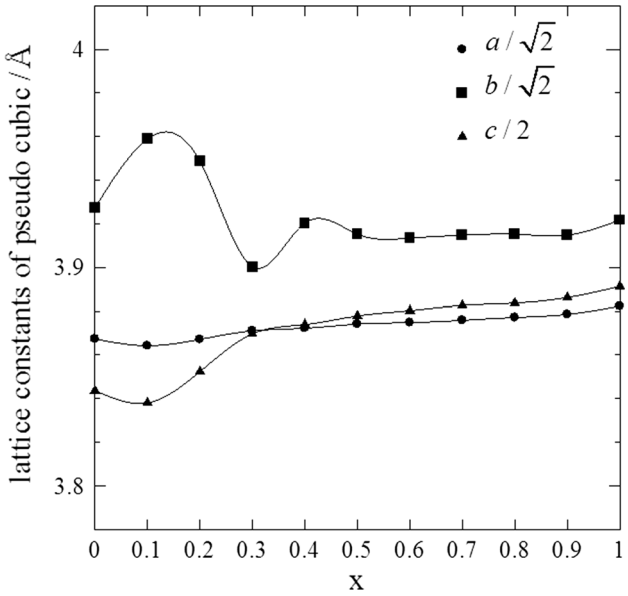

Fig. 2. Lattice parameters of pseudocubic $Pr_{0.9}Sr_{0.1}Mn_{1-x}Fe_xO_3$ ($0 \le x \le 1$) at room temperature.

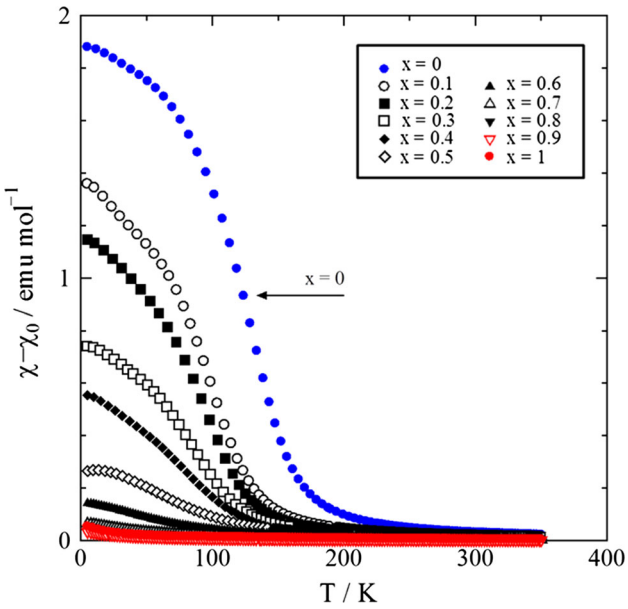

Fig. 3. Temperature dependence of dc magnetic susceptibility ($\chi - \chi_0$) for $Pr_{0.9}Sr_{0.1}Mn_{1-x}Fe_xO_3$ ($0 \le x \le 1$) under zero-field cooling conditions at magnetic field of 1 T during the warming process, where the temperature-independent term, χ_0, is evaluated from $\chi(T \to \infty)$.

(Table I). Even when the effect of polycrystallinity in the samples is taken into account, the calculated values of ω_{LO} are consistent with the typical optical phonon frequency, i.e., $\omega_{LO} \approx 10^{13}$ Hz to 10^{14} Hz.

Figure 7 shows the temperature dependence of S for the specimens with $0 \le x \le 1$ measured at temperatures up to 850 K. All samples showed large positive S below room temperature and a sharp fall up to 400 K, above which the positive S for $x \le 0.8$

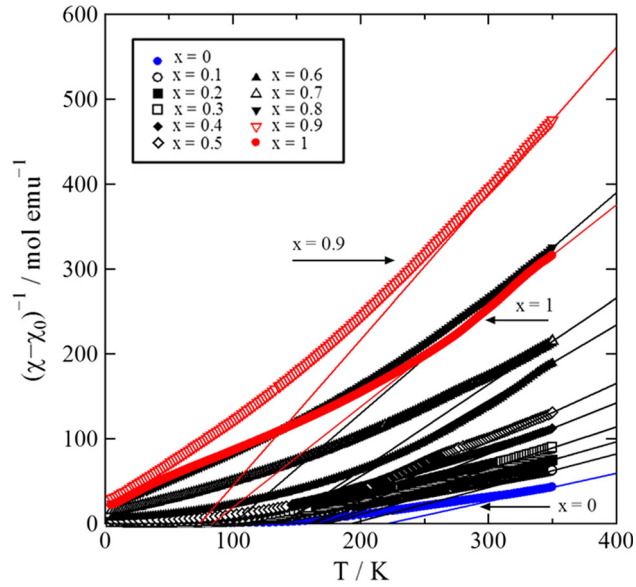

Fig. 4. Temperature dependence of inverse magnetic susceptibility $(\chi - \chi_0)^{-1}$ for $Pr_{0.9}Sr_{0.1}Mn_{1-x}Fe_xO_3$ ($0 \le x \le 1$). The straight lines represent the Curie–Weiss law above room temperature.

decreased gradually and approached zero. On the other hand, the positive S values for $x \ge 0.9$ maintained large absolute value, showing a gradual increase up to 850 K. For high-temperature extrapolation (Fig. 8), we assumed an expression for S above room temperature with T^{-1} dependence according to the following equation because of small polaron hopping conduction:[32]

$$S = S_\infty \pm \frac{k_B}{e}\frac{E_S}{k_B T}, \qquad (3)$$

where E_S ($\ll E_\sigma$) is the characteristic energy for the Seebeck coefficient, and S_∞ is the thermopower in the high-temperature limit, i.e., the temperature-independent term. Table III presents the results for E_S and S_∞ for the specimens with $0 \le x \le 1$ obtained from least-mean-squares fitting in Fig. 8. If we assume that the values of E_S correspond to $E_g/2$ in Eq. 2, the hopping energy can be expressed as $W_H = E_\sigma - E_S$.[9] The values of W_H for the samples with $0 \le x \le 1$ are also given in Table III.

According to an extended Heikes formula,[13,33] S_∞ for $Pr_{0.9}Sr_{0.1}Mn_{1-x}Fe_xO_3$ ($0 \le x \le 1$) can be expressed as

$$S_\infty = -\frac{k_B}{e}\ln\left(\frac{g_3}{g_4}\cdot\frac{x_4}{x_3}\right), \qquad (4)$$

where $x_3 = 0.9$, $x_4 = 0.1$, and g_3 and g_4 are the concentration of the trivalent ion, concentration of the tetravalent ion, degeneracy of the spin and orbital degrees of freedom of the trivalent ion, and degeneracy of the spin and orbital degrees of freedom of the tetravalent ion, respectively. Since Mn^{3+} and Mn^{4+} ions are in the HS state and e_g-level splitting occurs because of JT distortion of the

Table II. Temperature-independent magnetic susceptibility (χ_0), paramagnetic Curie temperature (Θ), Curie constant (C), effective magnetic moment (μ_{eff}), spin quantum number (S'), ionic ratios of B-site ions, and average ionic radii of A/B sites for $Pr_{0.9}Sr_{0.1}Mn_{1-x}Fe_xO_3$ ($0 \le x \le 1$)

Sample	$Pr_{0.9}Sr_{0.1}MnO_3$	$Pr_{0.9}Sr_{0.1}Mn_{1-x}Fe_xO_3$								$Pr_{0.9}Sr_{0.1}FeO_3$
Composition, x	0	0.1	0.2	0.3	0.4	0.5	0.6	0.7	0.8	0.9	1
χ_0 (emu mol^{-1})	0.00287(1)	0.00285(1)	0.00239(1)	0.00317(1)	0.002857(5)	0.00321(1)	0.003779(1)	0.00301(1)	0.003572(2)	0.005025(1)	0.007123(2)
Θ (K)	220.3(4)	192.2(4)	173.8(5)	168.9(4)	162.5(4)	159.7(3)	136.9(2)	138.0(4)	99.8(2)	73.9(1)	84.1(4)
C (emu K mol^{-1})	3.023	2.525	2.344	2.027	1.669	1.453	1.124	0.987	0.770	0.581	0.842
μ_{eff} (μ_B)	4.917	4.493	4.329	4.026	3.653	3.409	2.998	2.809	2.481	2.155	2.595
Spin quantum number, S'	2.01	1.80	1.72	1.57	1.39	1.28	1.08	0.99	0.84	0.69	0.89
High-spin Mn^{3+} (%)	90.0	80.2	74.8	67.4	54.4	47.6	33.0	29.1	18.8	8.8	–
High-spin Mn^{4+} (%)	10.0	9.8	5.2	2.6	5.6	2.4	7.0	0.9	1.2	1.2	–
Low-spin Fe^{3+} (%)	–	9.8	15.2	22.6	35.6	42.4	57.0	60.9	71.2	81.2	56.0
Intermediate-spin Fe^{3+} (%)	–	–	–	–	–	–	–	–	–	–	34.0
Low-spin Fe^{4+} (%)	–	0.2	4.8	7.4	4.4	7.6	3.0	9.1	8.8	8.8	10.0
Average ionic radius of B site (Å)	0.634	0.624	0.622	0.616	0.602	0.597	0.581	0.581	0.571	0.561	0.559
Average ionic radius of A site (Å)	1.205	1.205	1.205	1.205	1.205	1.205	1.205	1.205	1.205	1.205	1.205

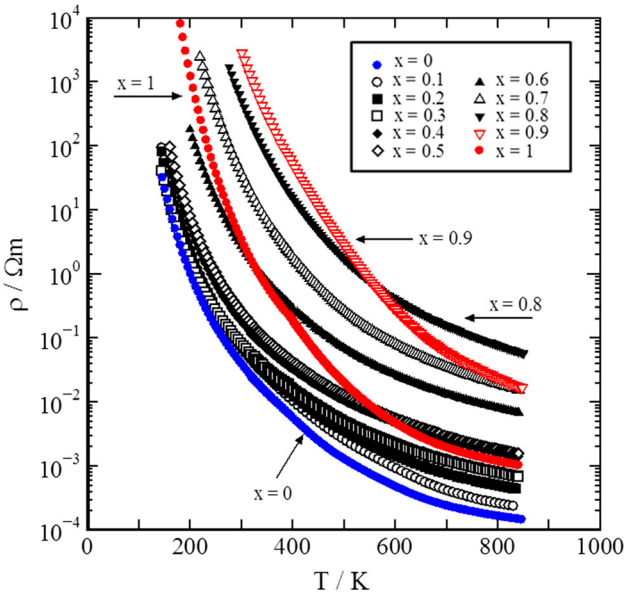

Fig. 5. Temperature dependence of electrical resistivity (ρ) for $Pr_{0.9}Sr_{0.1}Mn_{1-x}Fe_xO_3$ ($0 \le x \le 1$).

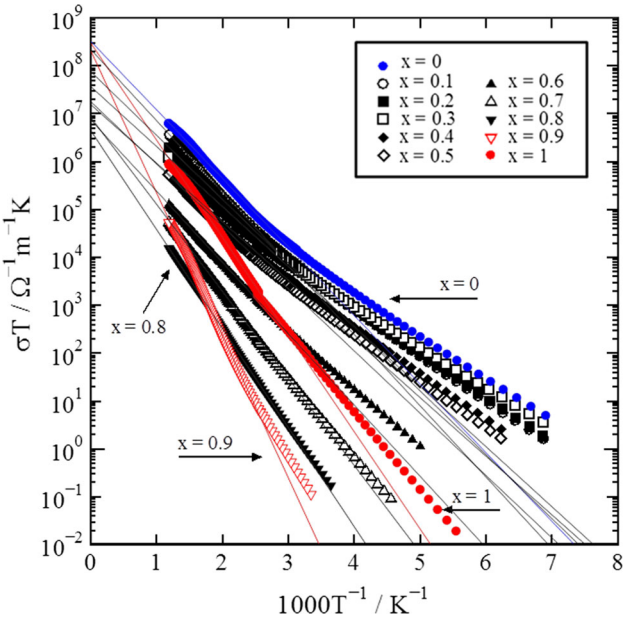

Fig. 6. Arrhenius relationship between σT and T^{-1} for $Pr_{0.9}Sr_{0.1}Mn_{1-x}Fe_xO_3$ ($0 \le x \le 1$) above 125 K. The straight lines represent the linear portions of the Arrhenius plots.

octahedral MnO_6,[24] $g_3 = 5$ due to the spin degeneracy of the $t_{2g}^3 e_g^1$ state and $g_4 = 4$ due to the spin degeneracy of the t_{2g}^3 state. Thus, S_∞ for $x = 0$ is calculated to be 170.1 μV K^{-1}. However, as shown in Fig. 8, negative $S_\infty = -69.9$ μV K^{-1} was obtained by extrapolating S to $T \rightarrow \infty$. We do not have a clear explanation for this discrepancy yet, but suspect that the thermopower for $x = 0$ may change sign in going from hole- to electron-like behavior

Table III. Activation energy of electrical conduction (E_σ), preexponential term (σ_0), concentration of tetravalent ions per unit volume (n_0), intersite hopping distance (a_0), optical phonon frequency (ω_{LO}), characteristic energy of Seebeck coefficient (E_S), hopping energy of small polarons (W_H), Seebeck coefficient in high-temperature limit (S_∞) evaluated from Heikes formula, bulk density at room temperature (d), relative density at room temperature, specific heat at room temperature (C_V), thermal diffusivity at room temperature (α), and thermal conductivity at room temperature (κ) for $Pr_{0.9}Sr_{0.1}Mn_{1-x}Fe_xO_3$ ($0 \le x \le 1$)

Sample	$Pr_{0.9}Sr_{0.1}MnO_3$	$Pr_{0.9}Sr_{0.1}Mn_{1-x}Fe_xO_3$				
Composition, x	**0**	**0.1**	**0.2**	**0.3**	**0.4**	**0.5**
E_σ (eV)	0.284	0.295	0.265	0.249	0.243	0.258
σ_0 (Ω^{-1} m^{-1} K)	$3.1(2) \times 10^8$	$2.0(3) \times 10^8$	$7.2(4) \times 10^7$	$3.5(2) \times 10^7$	$1.4(2) \times 10^7$	$1.6(2) \times 10^7$
Concentration of tetravalent ions, n_0 (m^{-3})	1.71×10^{27}	1.70×10^{27}	1.70×10^{27}	1.71×10^{27}	1.70×10^{27}	1.70×10^{27}
Intersite hopping distance, a_0 (Å)	3.96	3.98	3.96	3.95	3.97	3.97
Optical phonon frequency, ω_{LO} (THz)	$6.2(2) \times 10^2$	$3.9(6) \times 10^2$	$1.4(1) \times 10^2$	$7.1(4) \times 10^1$	$2.8(4) \times 10^1$	$3.2(4) \times 10^1$
E_S (eV)	0.057	0.068	0.098	0.092	0.044	0.086
W_H (eV)	0.227	0.227	0.167	0.157	0.199	0.172
S_∞ (μV K^{-1})	−69.92(5)	−79(1)	−109(1)	−100.7(2)	−39.1(3)	−80.0(1)
d (kg m^{-3}) at RT	6260	6306	6333	6062	6083	6062
Relative density (%)	92.3	93.4	94.0	89.3	90.2	89.9
C_V (J kg^{-1} K^{-1}) at RT	700	300	410	550	700	590
α (m^2 s^{-1}) at RT	2.49×10^{-7}	3.53×10^{-7}	3.20×10^{-7}	4.60×10^{-7}	3.36×10^{-7}	4.18×10^{-7}
κ (W m^{-1} K^{-1}) at RT	1.09	0.67	0.83	1.57	1.43	1.49

Sample	$Pr_{0.9}Sr_{0.1}Mn_{1-x}Fe_xO_3$				$Pr_{0.9}Sr_{0.1}FeO_3$
Composition, x	**0.6**	**0.7**	**0.8**	**0.9**	**1**
E_σ (eV)	0.296	0.361	0.411	0.590	0.403
σ_0 (Ω^{-1} m^{-1} K)	$7.0(2) \times 10^6$	$7.8(2) \times 10^6$	$4.1(1) \times 10^6$	$1.9(2) \times 10^8$	$2.8(2) \times 10^8$
Concentration of tetravalent ions, n_0 (m^{-3})	1.70×10^{27}	1.70×10^{27}	1.70×10^{27}	1.69×10^{27}	1.69×10^{27}
Intersite hopping distance, a_0 (Å)	3.97	3.99	3.98	3.98	3.99
Optical phonon frequency, ω_{LO} (THz)	$1.41(4) \times 10^1$	$1.55(4) \times 10^1$	8.2(2)	$3.8(4) \times 10^2$	$5.6(4) \times 10^2$
E_S (eV)	0.065	0.076	0.010	0.097	0.015
W_H (eV)	0.231	0.285	0.401	0.493	0.388
S_∞ (μV K^{-1})	−58.8(5)	−72.7(1)	2.3(1)	413.7(9)	157.7(3)
d (kg m^{-3}) at RT	6210	6029	6108	6317	6278
Relative density (%)	92.1	89.4	90.7	93.8	93.6
C_V (J kg^{-1} K^{-1}) at RT	610	600	570	390	300
α (m^2 s^{-1}) at RT	4.33×10^{-7}	6.13×10^{-7}	5.30×10^{-7}	1.17×10^{-6}	5.40×10^{-7}
κ (W m^{-1} K^{-1}) at RT	1.64	2.22	1.84	2.88	1.02

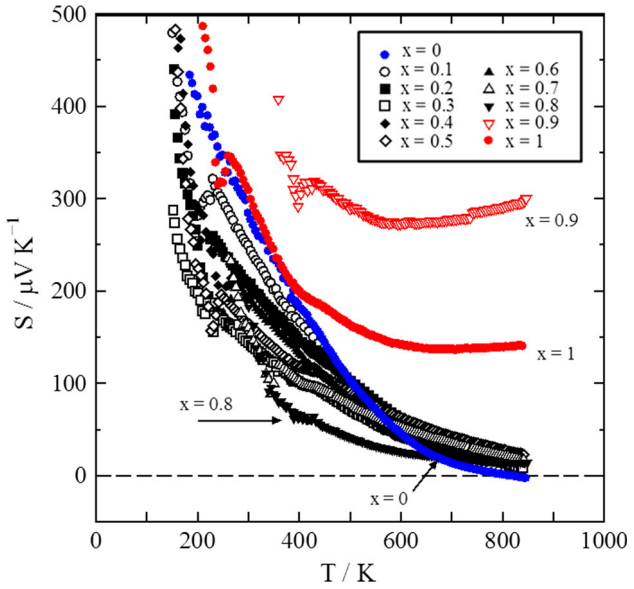

Fig. 7. Temperature dependence of Seebeck coefficient (S) for $Pr_{0.9}Sr_{0.1}Mn_{1-x}Fe_xO_3$ ($0 \le x \le 1$).

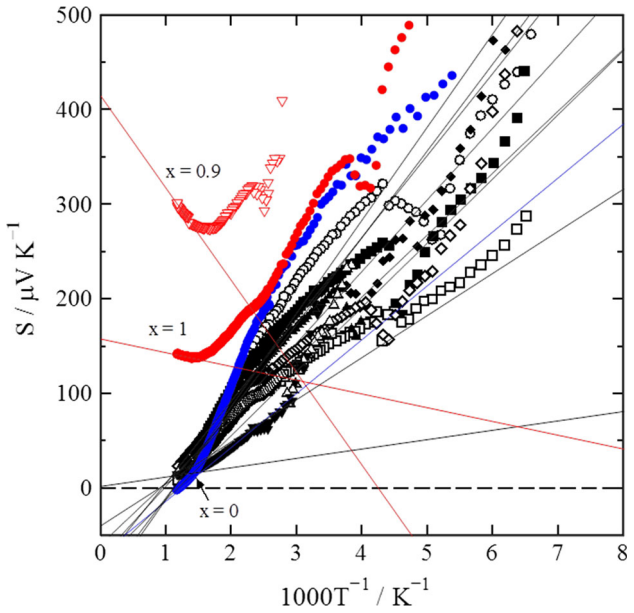

Fig. 8. Temperature dependence of Seebeck coefficient (S) for $Pr_{0.9}Sr_{0.1}Mn_{1-x}Fe_xO_3$ ($0 \le x \le 1$) above 125 K, where the straight lines represent the theoretical relationship of Eq. 3.

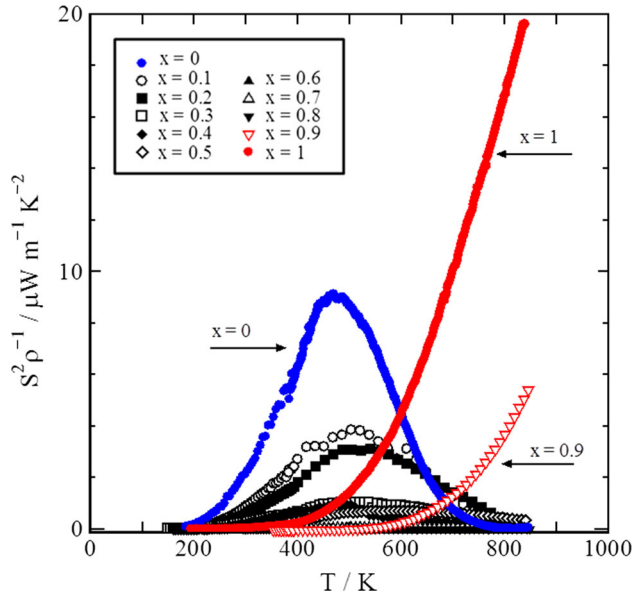

Fig. 9. Temperature dependence of power factor ($S^2\rho^{-1}$) for $Pr_{0.9}Sr_{0.1}Mn_{1-x}Fe_xO_3$ ($0 \le x \le 1$).

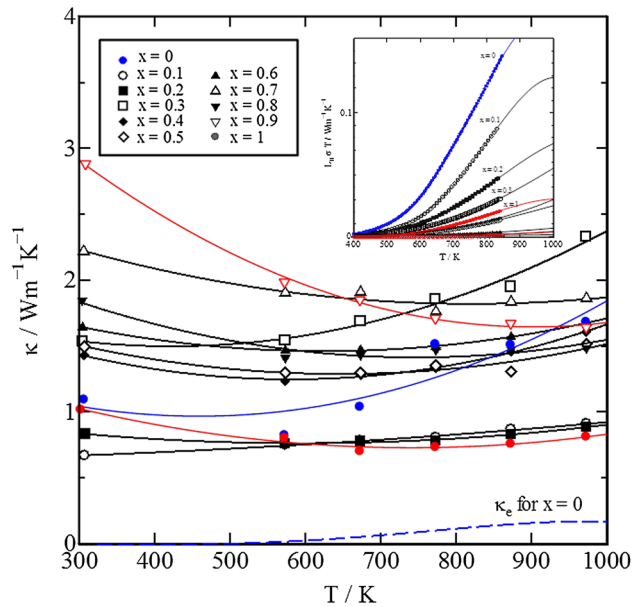

Fig. 10. Temperature dependence of total thermal conductivity ($\kappa = \kappa_L + \kappa_e$) above room temperature for $Pr_{0.9}Sr_{0.1}Mn_{1-x}Fe_xO_3$ ($0 \le x \le 1$). The inset shows the temperature dependence of the electronic thermal conductivity ($\kappa_e = L_0\sigma T$) above 400 K for $0 \le x \le 1$ using the well-known Wiedemann–Franz law.

above 800 K. On the other hand, since a part of the trivalent ions for $x = 1$ change from LS Fe^{3+} to IS Fe^{3+}, S_∞ for $x = 1$ is calculated to be

$$S_\infty = -\frac{k_B}{e}\ln\left(\frac{6}{9}\cdot\frac{0.100}{0.560}\right) - \frac{k_B}{e}\ln\left(\frac{24}{9}\cdot\frac{0.100}{0.340}\right) = 204.4\,\mu\mathrm{V\,K^{-1}}, \quad (5)$$

where g_3 for LS Fe^{3+}, g_3 for IS Fe^{3+}, and g_4 for LS Fe^{4+} are equal to 6, 24, and 9, respectively, owing to both the spin and orbital degeneracy. As shown in Fig. 8, this is in good agreement with the experimental value of $S_\infty = 157.7\,\mu\mathrm{V\,K^{-1}}$ for $x = 1$.

Figure 9 shows the temperature dependence of the power factor S^2/ρ calculated from the data for $0 \le x \le 1$ in Figs. 5 and 7 in the temperature range up to 850 K. S^2/ρ for $x = 0$ increases up to 467 K then decreases rapidly, reaching a maximum value of 9.5×10^{-6} W m^{-1} K^{-2} at 467 K. On the other hand, S^2/ρ for $x \ge 0.9$ increases monotonically with

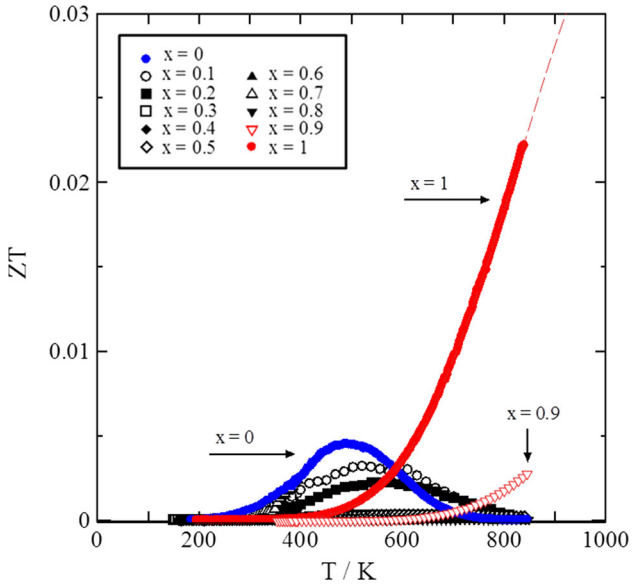

Fig. 11. Temperature dependence of dimensionless figure of merit (ZT) for $Pr_{0.9}Sr_{0.1}Mn_{1-x}Fe_xO_3$ ($0 \le x \le 1$).

increasing temperature, and the maximum S^2/ρ is 20×10^{-6} W m^{-1} K^{-2} at 850 K for $x = 1$. Above 700 K, the second S^2/ρ maximum is 5.5×10^{-6} W m^{-1} K^{-2} at 850 K for $x = 0.9$. The $x = 1$ specimen clearly showed the largest S^2/ρ of all the samples above 600 K.

Figure 10 shows the total thermal conductivity κ ($= \kappa_L + \kappa_e$), where κ_L and κ_e are the lattice thermal conductivity and electronic thermal conductivity, respectively. The electronic thermal conductivity is calculated by using the well-known Wiedemann–Franz law ($\kappa_e = L_0\sigma T$), where the Lorenz number L_0 is equal to 2.45×10^{-8} V^2 K^{-2}. κ_e is illustrated in the inset. Although κ_e increases with increasing temperature, the influence of κ_e on κ is much smaller than that of κ_L. For all specimens, κ_L is more significant than κ_e, so κ is mainly ascribed to κ_L. As shown in Fig. 10, κ_L for all the samples maintained small values of up to 3 W m^{-1} K^{-1} over the whole temperature range.

Finally, we present the ZT values for $0 \le x \le 1$ as a function of temperature. Figure 11 shows that ZT for $x \ge 0.9$ increased monotonically with increasing temperature. Clearly, the specimen with $x = 1$ exhibited the largest ZT of all the samples above 600 K. The largest ZT for $x = 1$ was 0.024 at 850 K, whereas the specimen with $x = 0$ showed maximum ZT of 0.005 at 467 K. This result indicates that hole-doped perovskite-type Fe oxides show p-type thermoelectric properties at high temperature, with relatively high Seebeck coefficient, moderate electrical resistivity, and low thermal conductivity.

CONCLUSIONS

Polycrystalline samples of $Pr_{0.9}Sr_{0.1}Mn_{1-x}Fe_xO_3$ ($0 \le x \le 1$) were synthesized by a conventional solid-state reaction,[9] and their crystal structure, magnetic properties, and thermoelectric properties investigated. All samples at 300 K showed single phase with orthorhombic perovskite structure in space group *Pbnm*. The Goldschmidt tolerance factor was observed to increase with increasing x because of the constant r_A, indicating that lattice parameters a and c slightly increased, in spite of the decrease in r_B. On the other hand, the BVSs of sites A and B were found to be about 2.9 and 3.1, respectively, corresponding to nominal ionic valence. The temperature dependence of the magnetic susceptibility suggested that ferromagnetism was suppressed with increasing x. In addition, with increasing x, most of the trivalent and tetravalent ions at B site changed from HS Mn^{3+} and HS Mn^{4+} to LS Fe^{3+} and LS Fe^{4+}, respectively. In particular, some of the trivalent ions for $x = 1$ changed from LS Fe^{3+} to IS Fe^{3+}. We concluded that the low-spin state of the Fe ions dominated the electronic structure for $x \ge 0.9$ and that all samples exhibited adiabatic small polaron behavior in their conduction mechanism above room temperature. In fact, the ω_{LO} values calculated from the Arrhenius relationship between σT and T^{-1} are consistent with the typical optical phonon frequency, i.e., $\omega_{LO} \approx 10^{13}$ Hz to 10^{14} Hz. We also confirmed that the positive S for $x \ge 0.9$ showed a gradual increase up to 850 K, and the predicted S_∞, as defined by the Heikes formula, for $x = 1$ was in good agreement with the experimental value of S_∞. The $x = 1$ specimen clearly showed the largest S^2/ρ of all the samples above 600 K. κ was mainly ascribed to κ_L, which maintained low values of up to 3 W m^{-1} K^{-1} over the whole temperature range. Thus, we obtained the largest ZT value of 0.024 at 850 K for $x = 1$. This indicates that hole-doped perovskite-type iron oxides exhibit p-type thermoelectric properties at high temperature, with relatively high Seebeck coefficient, moderate electrical resistivity, and low thermal conductivity.

ACKNOWLEDGEMENTS

This study was partly supported by MEXT KAKENHI (Grant No. 15K06479). The authors are very grateful to I. Ishikawa for his experimental assistance.

REFERENCES

1. I. Terasaki, Y. Sasago, and K. Uchinokura, *Phys. Rev. B* 56, R12685 (1997).
2. Y. Miyazaki, K. Kudo, M. Akoshima, Y. Ono, Y. Koike, and T. Kajitani, *Jpn. J. Appl. Phys.* 39, L531 (2000).
3. M. Ohtaki, T. Tsubota, K. Eguchi, and H. Arai, *J. Appl. Phys.* 79, 1816 (1996).
4. M. Yasukawa and N. Murayama, *Mater. Sci. Eng. B* 54, 64 (1998).
5. M. Ohtaki, H. Koga, T. Tokunaga, K. Eguchi, and H. Arai, *J. Solid State Chem.* 120, 105 (1995).
6. R. Funahashi, S. Urata, K. Mizuno, T. Kouuchi, and M. Mikami, *Appl. Phys. Lett.* 85, 1036 (2004).
7. R. Funahashi, M. Mikami, T. Mihara, S. Urata, and N. Ando, *J. Appl. Phys.* 99, 066117 (2006).
8. S. Urata, R. Funahashi, T. Mihara, A. Kosuga, S. Sodeoka, and T. Tanaka, *Int. J. Appl. Ceram. Technol.* 4, 535 (2007).

9. H. Nakatsugawa, M. Kubota, and M. Saito, *Mater. Trans.* 56, 864 (2015).
10. S. Ohta, H. Ohta, and K. Koumoto, *J. Ceram. Soc. Jpn.* 114, 102 (2006).
11. M. Iijima and N. Murayama, *Proc. Int. Conf. Thermoelectr.* ICT98, 598 (1998).
12. K. Iwasaki, T. Ito, T. Nagasaki, Y. Arita, M. Yoshino, and T. Matsui, *J. Solid State Chem.* 181, 3145 (2008).
13. W. Koshibae, K. Tsutsui, and S. Maekawa, *Phys. Rev. B* 62, 6869 (2000).
14. L. Pi, C. Martin, A. Maignan, and B. Raveau, *Phys. Rev. B* 67, 024430 (2003).
15. P.X. Thao, T. Tsuji, M. Hashida, and Y. Yamamura, *J. Ceram. Soc. Jpn.* 111, 544 (2003).
16. B.T. Cong, T. Tsuji, P.X. Thao, P.Q. Thanh, and Y. Yamamura, *Phys. B* 352, 18 (2004).
17. G. Xu, R. Funahashi, Q. Pu, B. Liu, R. Tao, G. Wang, and Z. Ding, *Solid State Ionics* 171, 147 (2004).
18. M. Miclau, S. Hebert, R. Retoux, and C. Martin, *J. Solid State Chem.* 178, 1104 (2005).
19. D. Flahaut, T. Mihara, R. Funahashi, N. Nabeshima, K. Lee, H. Ohta, and K. Koumoto, *J. Appl. Phys.* 100, 084911 (2006).
20. L. Bocher, M.H. Aguirre, D. Logvinovich, A. Shikabko, R. Robert, M. Trottmann, and A. Weidenkaff, *Inorg. Chem.* 47, 8077 (2008).
21. R. Helmolt, J. Wecker, B. Holzapfel, L. Schultz, and K. Samwer, *Phys. Rev. Lett.* 71, 2331 (1993).
22. A. Urishibara, Y. Morimoto, T. Arima, A. Asamitsu, G. Kido, and Y. Tokura, *Phys. Rev. B* 51, 14103 (1995).
23. C. Zener, *Phys. Rev.* 82, 403 (1951).
24. A. Maignan, C. Martin, F. Damay, and B. Raveau, *Phys. Rev. B* 58, 2758 (1998).
25. F. Izumi and K. Momma, *Solid State Phenom.* 130, 15 (2007).
26. R.D. Shannon, *Acta Crystallogr. Sect. A* 32, 751 (1976).
27. V.M. Goldschmidt, *Naturwissenschaften* 21, 477 (1926).
28. I.D. Brown, *Chem. Rev.* 109, 6858 (2009).
29. D. Emin and T. Holstein, *Ann. Phys.* 53, 439 (1969).
30. I.G. Austin and N.F. Mott, *Adv. Phys.* 18, 41 (1969).
31. L. Murawski, C.H. Chung, and J.D. Mackenzie, *J. Non-cryst. Solids* 32, 91 (1970).
32. T.T.M. Palstra, A.P. Ramirez, S.-W. Cheong, B.R. Zegarski, P. Schiffer, and J. Zaanen, *Phys. Rev.* B56, 5104 (1997).
33. R.R. Heikes and R.W. Ure, *Thermoelectricity: Science and Engineering* (New York/London: Interscience, 1961).